Electronic Supplementary Material (ESI) for Dalton Transactions
This journal is © The Royal Society of Chemistry 2012

Electronic Supplementary Information

Contents:

Elemental analysis

Samples of **1** wrapped in tin foil were prepared for elemental analysis in an Ar filled glovebox, keeping their exposure to air to a minimum. Samples of **1**·2H_2O were prepared in air. The samples were measured on a Vario EL III made by Elementar, at IChO PAN, Warsaw, Poland.

This journal is © The Royal Society of Chemistry 2012

Simulataneous thermogravimetric analysis and scanning calorimetry

Cycling experiments

Cycling experiments were carried out on a Netzsch STA 409 PG instrument, using thermogravimetric analysis and differential scanning calorimetry with a static air environment. Approximately 7 mg of **1**·2H_2O was loaded into an alumina crucible and heated up to 100 °C at a rate of 0.5 K min^{-1} and held at 100 °C for 2 hours to dehydrate the sample, then cooled to 30 °C at a rate of 0.5 K min^{-1} and held at room temperature for 8 hours to allow the sample to rehydrate. This procedure was repeated four times. The results (Figure S 1) demonstrate the reversibility of the **1** ⟷ **1**·2H_2O system. The small decrease in the maximum mass on each cycle is, we believe, a result of the limited availability of water in the closed TGA/DSC chamber, as on exposure to air outside the chamber the sample regained its original mass after a few minutes.

The nature of the experiment requires changes in the temperature ramp (from +0.5 K min^{-1} to steady 100 °C to -0.5 K min^{-1} to steady 30 °C), but this complicates analysis of the mass loss. Precise correction for this by running a blank experiment was not possible, but it is clear from Figure S 1 that the mass loss seen is close to the 7% expected for dehydration of **1**·2H_2O.

The DSC shows the double peak mentioned in the main paper on both dehydration and rehydration.

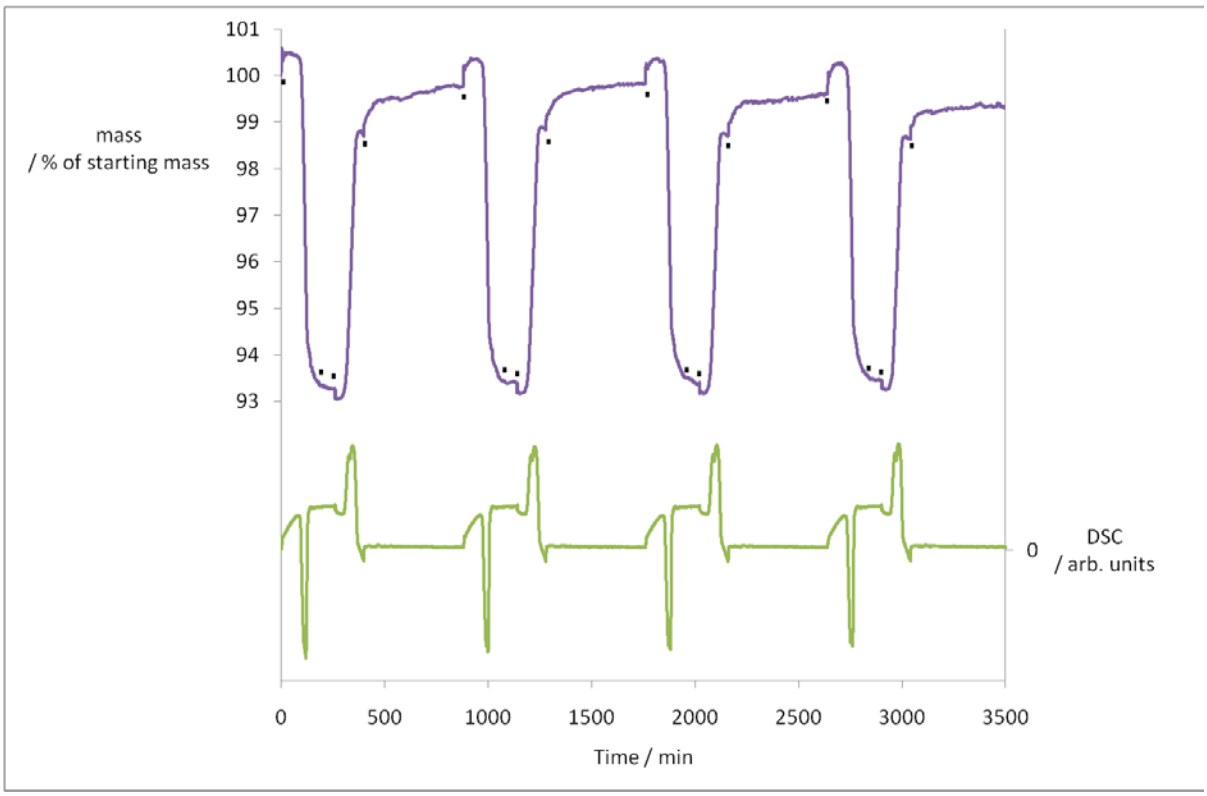

Figure S 1 Cycling experiment showing mass changes and DSC. Black dots show the points at which a change in the temperature ramp occurred, resulting in small but abrupt changes in the mass signal which are solely an artifact of the experimental method.

Figure S 2 shows a detailed measurement demonstrating the reversibility of dehydration/hydration. The cooling (hydration) process showed the same magnitude of enthalpy change as heating (dehydration). In addition, the cooling process gave better resolution of the two processes which we ascribe to hydration of first one water and then the second, allowing separate integration of the signals. The division (approximately 60:40 ratio for the low *T*:high *T* division of enthalpy change, i.e. 79 : 60 kJ mol^{-1}) is the same as that estimated for the heating peaks at slow scanning rates, where the peaks do not separate quite as well.

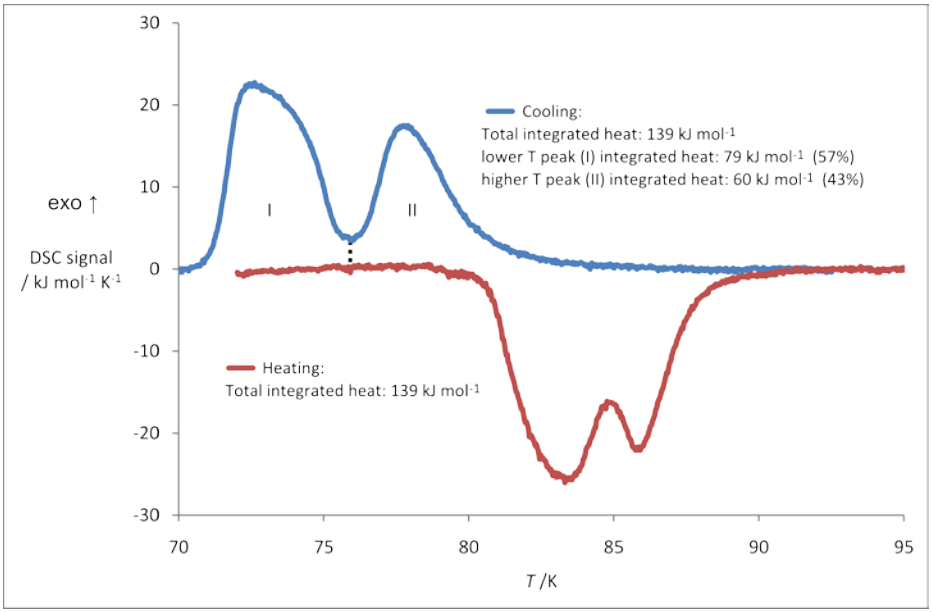

Figure S 2 DSC measurement showing heating of **1**·$2H_2O$ at 0.07 K min^{-1} followed by cooling of **1** (formed in situ) at 0.07 K min^{-1}, regenerating **1**·$2H_2O$. The magnitude of the enthalpy change is the same (within experimental error) in both. The cooling peaks are sufficiently well resolved to allow their separate integration, divided at the dotted line.

It might be expected that upon dehydration, loss of the first water (low *T* peak) would result in a lower enthalpy change than loss of the second water: when the first water leaves, the Ni(II) cation would bind the second water molecule more strongly. That this isn't the case suggests that an additional energy penalty is being paid, perhaps in terms of crystal packing, poorer hydrogen bonding or a less stable 5-coordinate complex.

Hydration can be interpreted in a similar manner but in reverse.

(NB, the data in Figure S 2 was recorded when conditions of humidity were different from previous measurements (we have no way to control the humidity inside the TGA/DSC chamber when using static air), which causes the slight change in the onset temperature for dehydration from that shown in the main paper.)

This journal is © The Royal Society of Chemistry 2012

Entropy change

An estimate of the entropy change on dehydration can be derived for each peak individually by assuming that at the slowest scanning speeds the conditions approximate thermodynamic equilibrium. Then,

$$\Delta S = \Delta H / T \qquad (1)$$

where ΔS and ΔH are change in entropy and change in enthalpy of reaction, respectively, while T is the absolute temperature at which reaction occurs. Qualitatively, we can see from equation (1) that the entropy change of the second water loss must be smaller than the first, given that for the second water loss, ΔH is smaller and T is larger, thus ΔS is required to be smaller.

Using data for the slowest scanning speed, 0.02 K min^{-1}, the first water lost has enthalpy change of 79±3 kJ mol^{-1}, and T was taken as 355±2 K (the process occurred over the range 353–357 K). This gives ΔS = 222±8 J mol^{-1} K^{-1} for the first peak. The second peak was calculated using ΔH = 60±3 kJ mol^{-1} and T = 358±2 K, giving ΔS = 167±8 J mol^{-1} K^{-1} for the second peak. For the overall process, **1**·2H_2O → **1** + 2 H_2O one obtains an average *per 1 molecule of evolved water* of ΔS = 195±8 J mol^{-1} K^{-1} , fairly close to the value of the standard entropy of water vapour (ca. 189 J mol^{-1} K^{-1}).[1] The absolute values must be treated with caution as the measurements were not made under standard conditions (1 atm H_2O vapour), nor was the humidity of the DSC chamber directly measured. Change in entropy is a function of water vapor pressure (as we saw in measurements made under different conditions of atmospheric humidity, with varying T of dehydration), so that comparison with other systems is difficult. However, the magnitudes are not out of kilter with that for elimination of gaseous water, as specified above.

The relative values for the two peaks, however, are of interest. The greater entropy change for the loss of the first water may be explained by considering two contributions: that of the first water moving to the gas phase (the main contribution), and the increased freedom experienced by the complex (particularly the remaining water) in the coordinatively unsaturated, 5 coordinate complex (**1**·1H_2O). When the *second* water enters the gas phase, it moves from a state that was less restricted (i.e. had higher entopy) than the first, and thus experiences a smaller entropy gain in the process.

To estimate the increased entropy, ΔS_{int}, of the proposed **1**·1H_2O against **1**·2H_2O, we may consider as a baseline the situation if the entropy increase was split evenly over the two water loss steps. In this case, the entropy increase for each water would be ΔS = (222 + 167) /2 = 195 J mol^{-1} K^{-1}. Given that we see ΔS = 222±10 J mol^{-1} K^{-1}, this suggests that, to a first approximation, ΔS_{int} = 27 J mol^{-1} K^{-1} (see Figure S 3). We have not attempted to propagate the errors, as this is only intended to be a very approximate value. Since, according to the Jenkins–Glasser approach, entropy is directly proportional to volume,[2] we infer that ΔS_{int} of 27 J mol^{-1} K^{-1} is equivalent to the approximate volume of one H_2O molecule in the condensed phase. This extra room is probably an empty coordination site which opens up after the first molecule of water has left the 6-coordinated **1**·2H_2O.

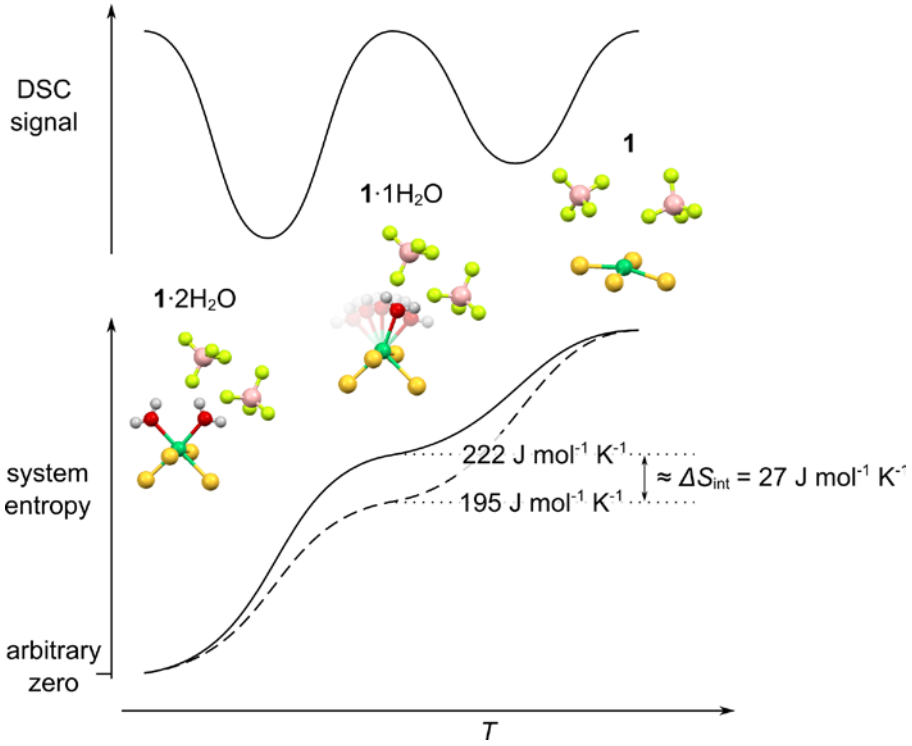

Figure S 3 Schematic diagram illustrating the calculation of the inferred increased entropy, $\Delta S_{int,}$ for the proposed species $1{\cdot}1H_2O$. The DSC signal (top) shows the lower *T* water loss step has a higher ΔH associated with it than the higher *T* step. The molecular species are shown in the middle. The system entropy (bottom), with an arbitrary zero set at the onset of the first water loss, shows the difference between the 'baseline' case (dashed line), where entropy change is equal for the two water loss steps, and the measured result (solid line), in which the lower *T* step shows a greater entropy change than the higher *T* step. ΔS_{int} supposedly comes from new degrees of freedom available to the remaining water molecule in a local 5-coordinate geometry of Ni after the first water molecule has been lost from $\mathbf{1}{\cdot}2H_2O$.

UV/vis spectroscopy

Time resolved UV/vis reflectance spectra were recorded on a Shimadzu UV-2401PC spectrometer fitted with a specular reflectance attachment. A thin pellet of **1**·2H_2O was formed and then dehydrated at 120 °C. This was allowed to rehydrate whilst the spectra (Figure S 4) were collected. This re-hydration was considerably slower for the highly compacted pellet than for powder, taking approximately 20 minutes to complete (see also a time-lapse video available online and Figure S 5).

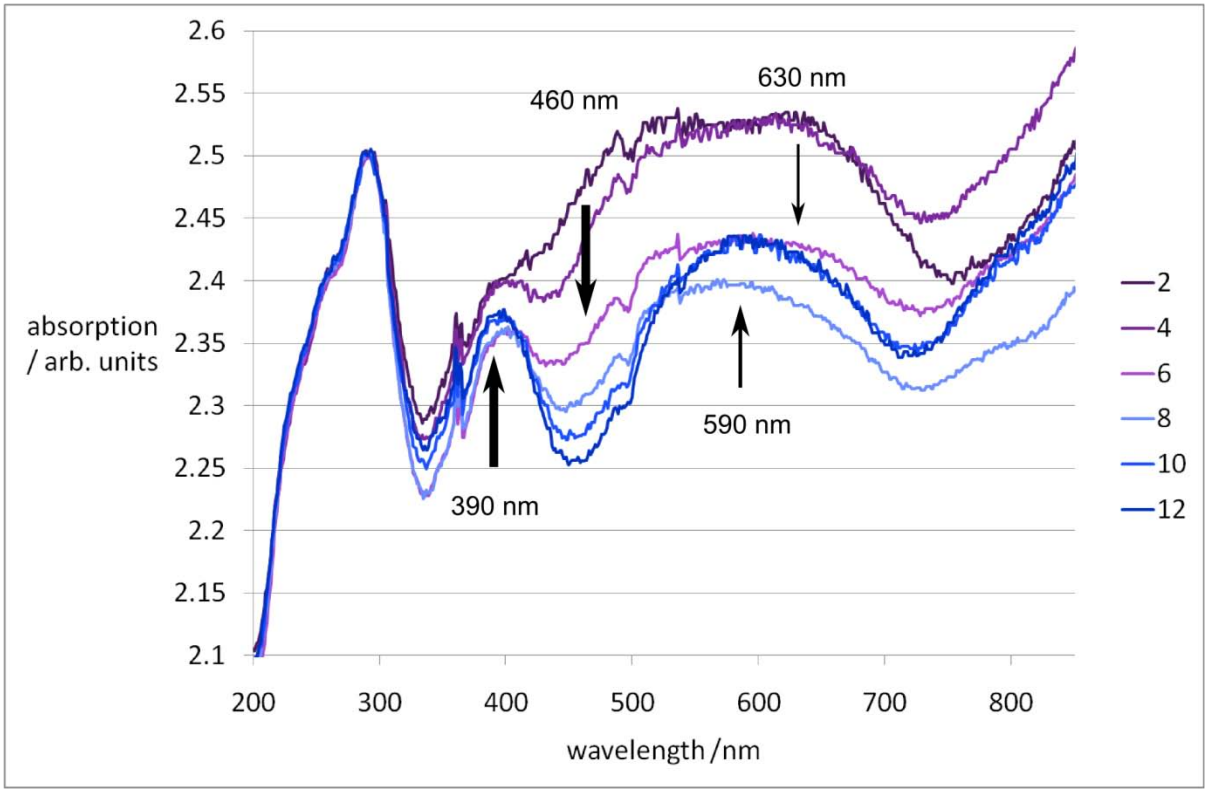

Figure S 4 Series of UV/vis spectra recorded whilst a pellet of **1** converted to **1**·2H_2O in air.

The UV/vis spectra in Figure S 4 have been normalized at 290nm. Arrows show decreases or increases in intensity upon conversion from purple to blue. The thickness of the arrow corresponds to clarity of the signal change.

The measurement of the first spectrum was started 2 min 10 sec after removal from the hotplate and each took 1 min 22 sec to complete. For clarity, only every other spectrum is shown with the final spectrum ('12') starting measurement approximately 21 min 40 sec after removal from the hotplate.

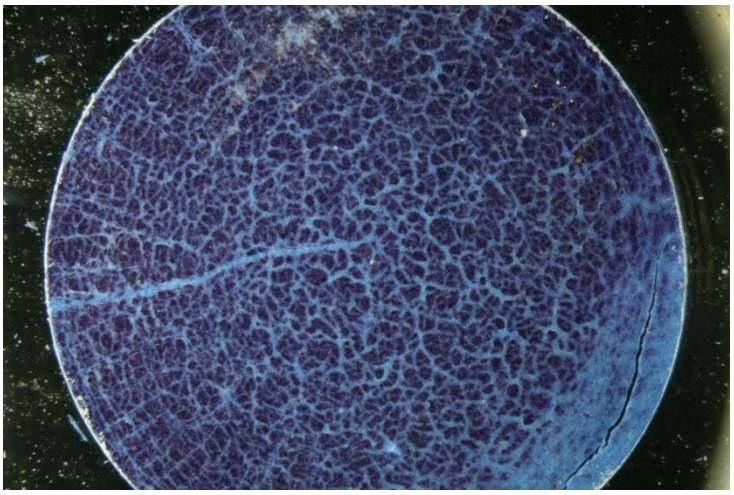

Figure S 5 Partially converted pellet used for UV/vis spectroscopy as seen under a microscope.

Powder X-ray diffraction

The indexing suggested that the synchrotron diffraction pattern of $1 \bullet 2H_2O$ contained an impurity, which was confirmed when a diffraction pattern from laboratory Co-target X-rays was obtained without the spurious peaks, however, structure solution from the synchrotron data with the impurity was still better than the poorer quality laboratory data.

The H positions were not refined, so no detailed H-bonding analysis has been done, however, it's not hard to speculate that H attached to O1 may H-bond to F4 and F8, and H attached to O2 with F6 and F2, which would form a ring of 8 H-bonds (see Figure S 6). H…F distances can be approximated by subtracting the typical O-H bond distance (0.82 Å) used in crystallographic software (eg Jana2006, ShellX) from the O…F distance, giving ranges of 1.8-1.9 Å.

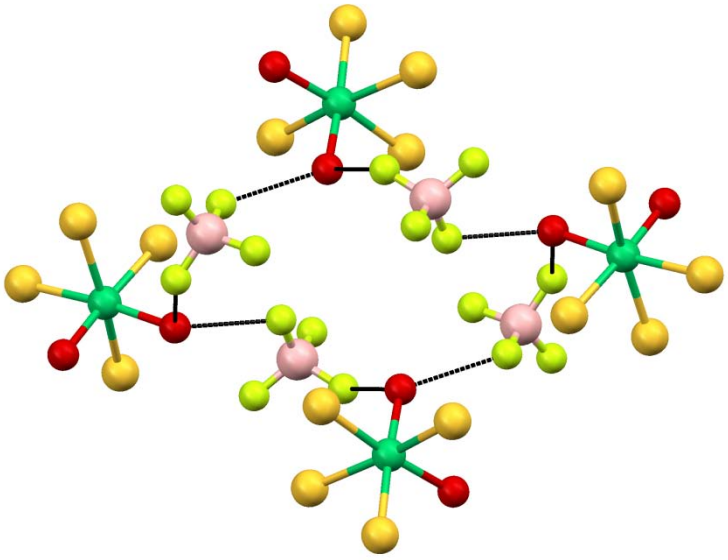

Figure S 6 View of hydrogen bonding 'ring' shown as black lines between O and F atoms (under the assumption that the undetermined H positions would be along or close to those lines). Hydrogen-bond lengths would be approximately 1.8 – 1.9 Å. Ni – green, S – gold, O – red, B – pink, F – yellow. C atoms have been omitted for clarity, H atoms have been omitted as their positions were not explicitly determined.

VESTA[3] and Mercury[4] were used for structure drawings.

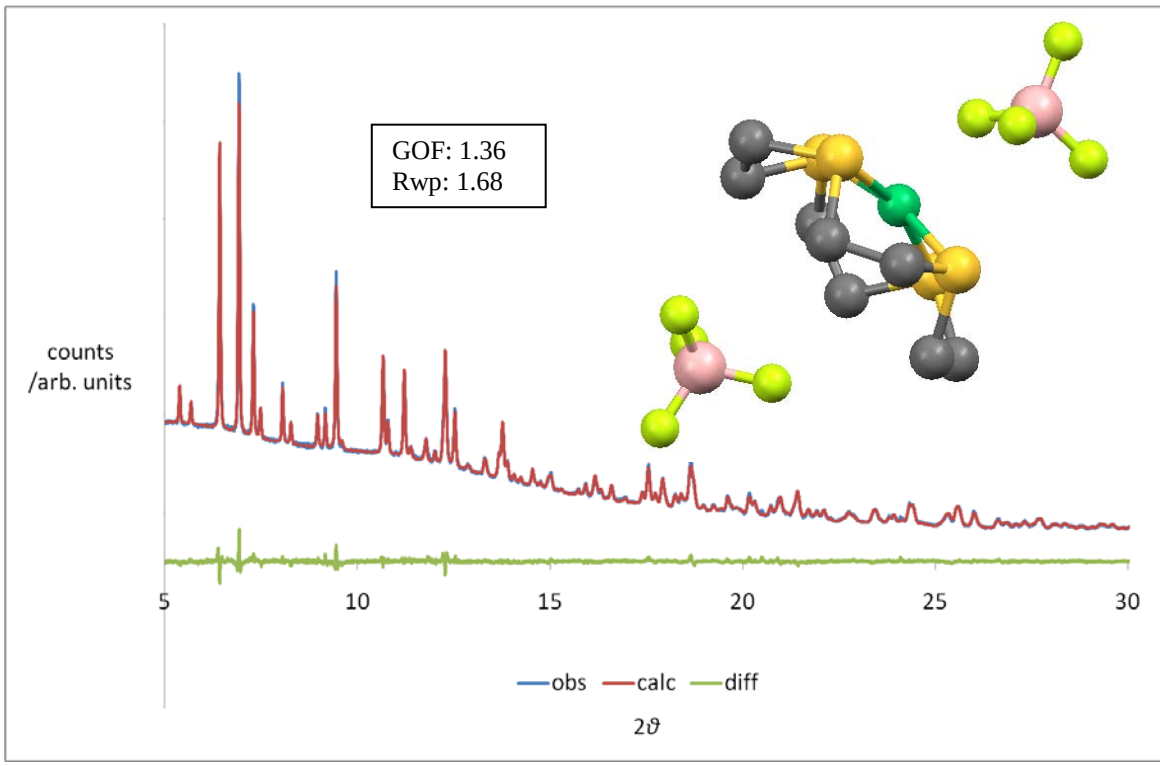

Figure S 7 Experimental (blue), calculated (red) and difference (green) powder diffraction patterns of **1**, together with the final refined molecular structure.

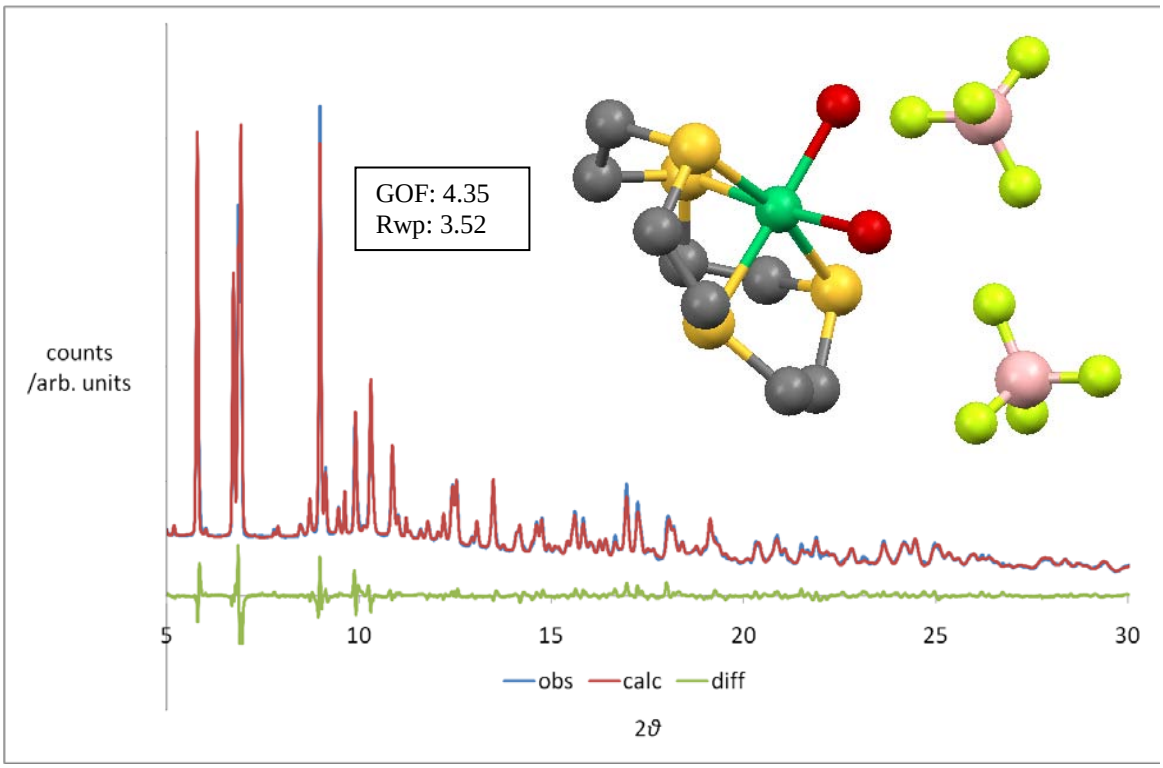

Figure S 8 Experimental (blue), calculated (red) and difference (green) powder diffraction patterns of **1**·2H_2O, together with the final refined molecular structure. This is the result after Rietveld refinement of the theoretical structure. Note, the poorer fit as compared to **1** is due to an impurity which it has not been possibly to identify or even to index.

The agreement between model and experiment for **1** was excellent (see Figure S 7). The apparently poor fit for **1**·2H_2O (see Figure S 8) that might be inferred from the fitting parameters is due to an unidentified and unindexed impurity. It was possible to track a number of peaks belonging to this phase using the temperature resolved patterns, and so to recognize where they cause problems, but it has not been possible to eliminate them. The poor parameters also reflect the otherwise extremely high quality synchrotron data, that is, the quality of the data is very unforgiving of even small 'errors' in the structure. Nevertheless, the chemical and structural agreement with that found for **1** (for which a very good fit was found) make us confident of its validity. Minor imperfections in the structure might nevertheless be present due to the mis-allocation of electron density owing to the impurity.

Analysis of C-C, C-S bond lengths and C-S-C, C-C-S angles in previously reported structures

Typical bond lengths and angles involving C and S in the 12aneS_4 ring (Figure S 9) were determined by examining structures in the Cambridge Structural Database[5] containing the 12aneS_4 motif or derivatives of it. The C-C and C-S bond lengths and C-S-C and C-C-S angles directly involved in the 12aneS_4 motif were extracted from each structure and then assessed for their relevance to the analysis. Where significant structural differences were found (e.g. 5 member rings, fused rings) or where the correct value was not apparent (e.g. with significant disorder) the bond length or angle was omitted from the analysis. In some crystals the same 12aneS_4 motif was repeated in the unit cell, in which case the bond lengths and angles were only counted once. After this process, the data from 51 structures was used, giving 277 C-C and 559 C-S bond lengths and 284 C-S-C and 583 C-C-S angles. Further details may be obtained from the authors on request. This analysis was used to inform the soft constraints used in the Rietveld refinement.

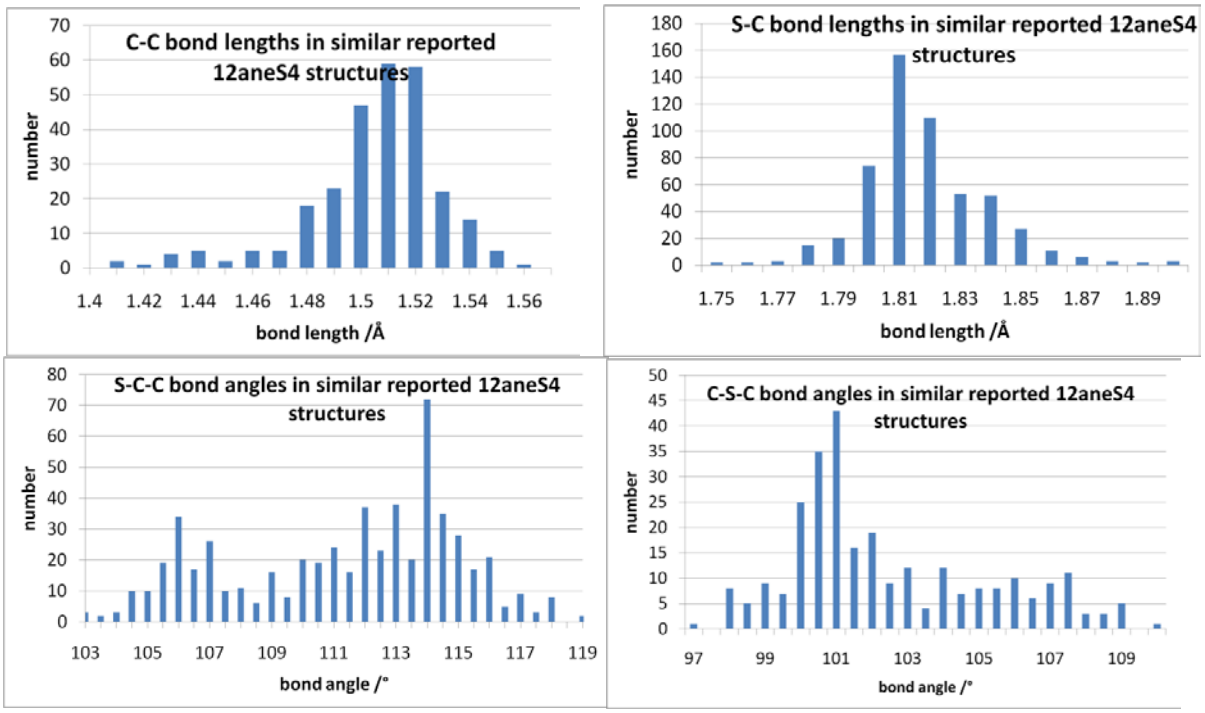

Figure S 9 Bond lengths and angles in reported similar structures containing 12aneS4 or derivatives (a few additional outlying data points are not shown)

This journal is © The Royal Society of Chemistry 2012

IR and Raman spectra

Recording the infrared spectra of **1** and **1**·2H_2O (Figure S 10) proved surprisingly challenging. The complexes were found to react with KBr forming a green compound, presumably through anion exchange forming Ni(12aneS_4)Br_2 or a similar complex. The answer for **1**·2H_2O (a very soft material) was to record the spectrum by pressing a thin film on AgCl windows and placing it in a sealed sample holder (to prevent dehydration in the evacuated sample chamber). However, **1** was too mechanically hard to form a suitable layer and simply using a powder gave a very poor result. The spectrum recorded in light mineral oil was of reasonable quality, but the particularly interesting C-H stretching region was obscured by the oil. To investigate this region, a thin film of **1**·2H_2O was prepared on AgCl windows and converted in situ to **1** by exposing the film to the evacuated sample chamber. The spectrum agreed well with that recorded in mineral oil, though slight residual O-H vibrations remained.

The results show clear differences in the fingerprint region (Figure S 10, bottom right). Slight shifts to lower frequency vibrations upon hydration are seen in the C-H stretching region. A clear change in the magnitude of the O-H stretching and bending regions demonstrates the loss of water. Why there is a slight residual signal in **1** is unclear, but it is not seen in the spectrum recorded in mineral oil and so is believed to be an artifact of the sample preparation (in situ dehydration, see above). There is no clearly discernible change in the B-F stretches of the hydrated sample, despite the establishment of H-bonding upon the introduction of water.

All IR spectra were recorded on a Bruker Vertex 80v spectrometer with vacuum sample chamber.

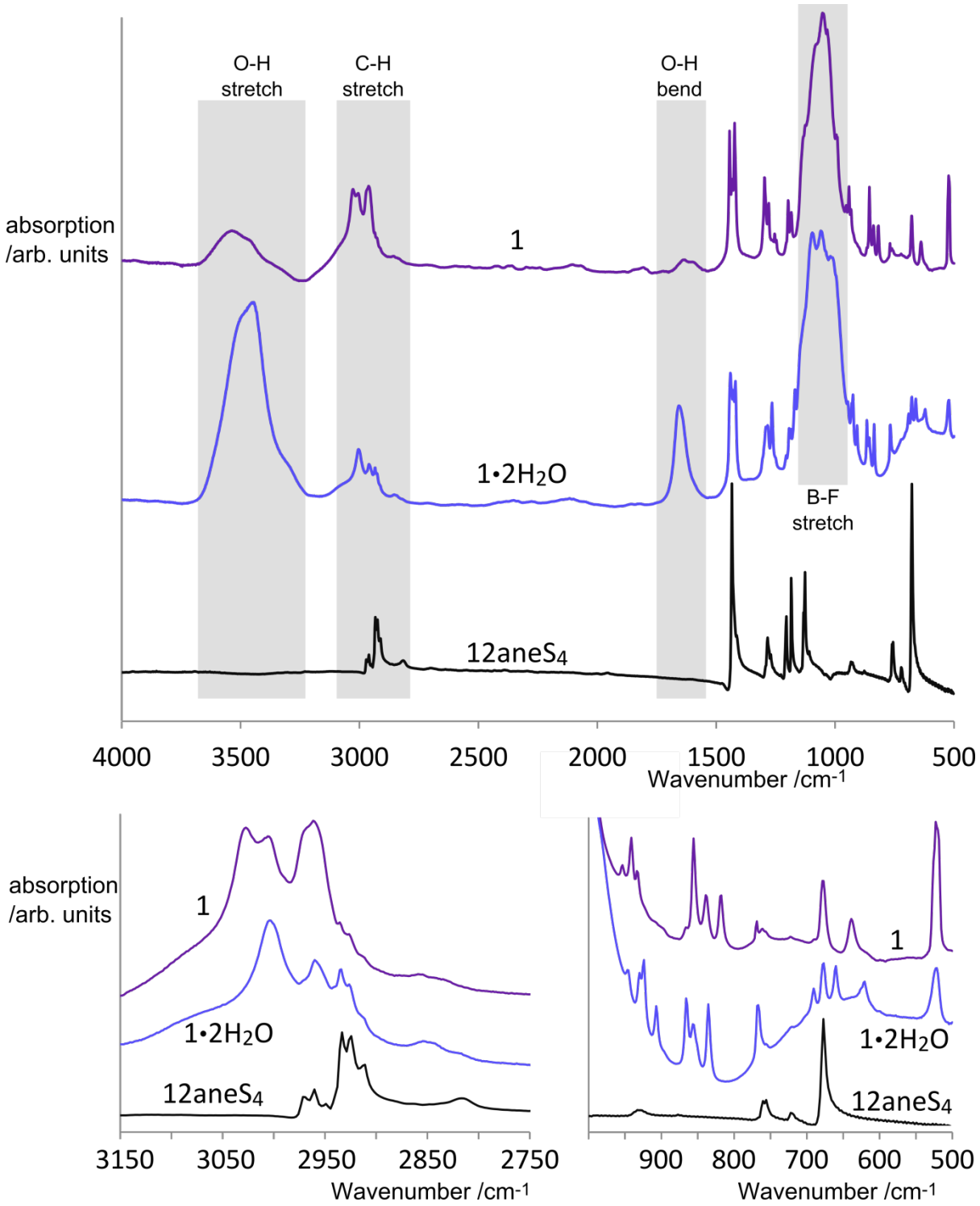

Figure S 10 Infrared spectra of **1**, **1**·2H_2O, and the 12aneS_4 reagent, with expanded detail for the C-H stretching region (bottom left), and the low frequency region (bottom right).

This journal is © The Royal Society of Chemistry 2012

The Raman spectra shown in Figure S 11 were collected in the backscattering configuration with a Labram HR800(Horiba Jobin–Yvon) confocal microscope system equipped with a Peltier-cooled CCD detector (1024 x 256 pixel) using a diode pumped, frequency doubled Nd:YAG laser (1064, 532 nm) and a 20mW He-Ne laser (633 nm). Calibration of the instrument was performed using the 520 cm^{-1} Raman signal of a silicon wafer. Spectra were obtained using a 50x magnification Olympus objective, a confocal pinhole size of 200 µm and a holographic grating with 600 grooves/mm. The complexes decomposed quickly even on moderate laser illumination at 532 nm, 633 nm and 1064 nm wavelengths, so heavy filters (100x reduction) and short collection times were necessary, limiting the signal to noise ratio achievable.

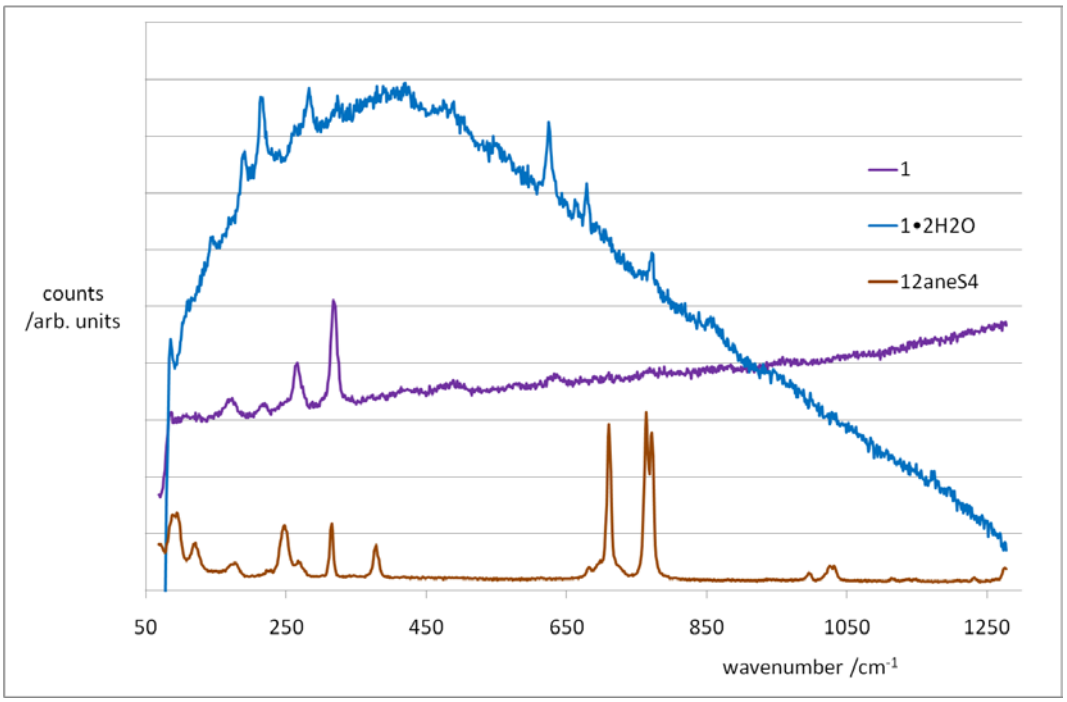

Figure S 11 Raman spectra of **1**, **1**·$2H_2O$, and the $12aneS_4$ reagent, collected with 633 nm wavelength laser irradiation. The spectrum of **1**·$2H_2O$ shows strong fluorescence which suggests a pre-resonance character for the Raman spectrum

DFT calculations

DFT calculations were carried out for both an isolated Ni(II)(12aneS$_4$)$^{2+}$ cation (and its mono- and di-hydrated forms) as well as for Ni(II)(12aneS$_4$)(BF$_4$)$_2$ (and its mono and di-hydrated forms) in the solid state. VESTA and Materials Studio[6] were used for structure drawings.

The molecular calculations were performed with Gaussian'09[7].The full geometry optimizations at the B3LYP/6-311++G** level were carried out for Ni(II)(12aneS$_4$)$^{2+}$ free of BF$_4^-$ counterions, Ni(II)(12aneS$_4$)(H$_2$O)$^{2+}$, and Ni(II)(12aneS$_4$)(H$_2$O)$_2^{2+}$ moieties, for two distinct spin states (low-spin singlet, high-spin triplet). The calculations revealed that for Ni(II)(12aneS$_4$)$^{2+}$ the ground state is a low-spin singlet, while for both hydrated forms the ground state is a high-spin triplet (Figure S 12). This means that spin crossover takes place upon addition of the first water molecule. The calculated energies of attachment of the first and second water molecules are –101.3 kJ/mol H$_2$O, and –72.3 kJ/mol H$_2$O, respectively, leading to the zero-point corrected energy of **1** + 2 H$_2$O→ **1**·2H$_2$O transformation of –173.6 kJ/mol Ni(II). This value is overestimated by ca. 36.7% with respect to experimental value mostly due to the fact that the Ni(II)(12aneS$_4$)$^{2+}$ carries unbalanced positive charge, so it is more easily ligated by water molecules.

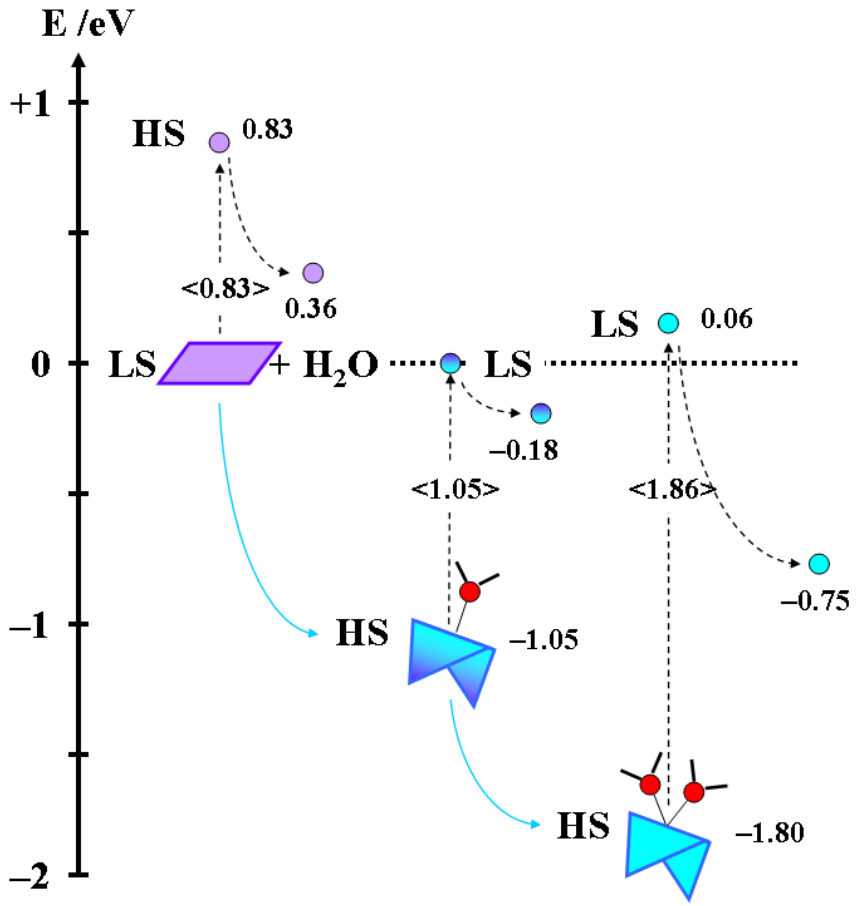

Figure S 12 Energy landscape for the **1** + 2 H$_2$O → **1**·2H$_2$O transformation (molecular DFT calculations). Vertical dashed arrows represent **vertical** electronic excitations; curved dashed arrows stand for **geometry relaxations** of the excited electronic state; blue arrows represent **chemical reactions** for step-by-step attachment of water molecules; **HS** is high-spin (2 unpaired electrons), **LS** is low spin (0 unpaired electrons).

The solid state DFT calculations were performed using Vienna ab initio Simulation Package (VASP) formally for p=0 Pa and T=0 K.[8] We used the local density approximation (LDA) and the projector augmented wave (PAW) method[9]. The wave functions were expanded in plane waves up to the kinetic energy cutoff of 400 eV providing good energy convergence (for water molecule in a box cutoff increase to 600 eV yielded energy improvement by 1 meV per FU, while increase to 900 eV by additional 9 meV per FU). The unit cell vectors for (i) **1**, (ii) **1**·2H_2O, (iii) hexagonal ice and (iv) a single water molecule inside a 10 Å x 12 Å x 12 Å box (representing a free molecule in a gas phase), were frozen at their experimental values, and all atomic positions were fully relaxed with the electronic and ionic convergence criteria set to 10^{-7} and 10^{-5} eV, respectively, and k-mesh spacing via the Monkhorst–Pack scheme with uniform spacing of 0.4 $Å^{-1}$. The pseudopotential representation was consistently in real and not in reciprocal space due to the size of the primitive unit cells of **1** and **1**·2H_2O. For **1**·2H_2O hydrogen atoms (not seen by x-ray methods) were added. Proposing reasonable initial positions for H atoms was straightforward as the topology of O…F distances clearly suggested the presence of one-center O-H…F hydrogen-bonds (Figure S 13). Optimizations led to very good reproduction of fractional atomic coordinates and bond lengths (Table 1).

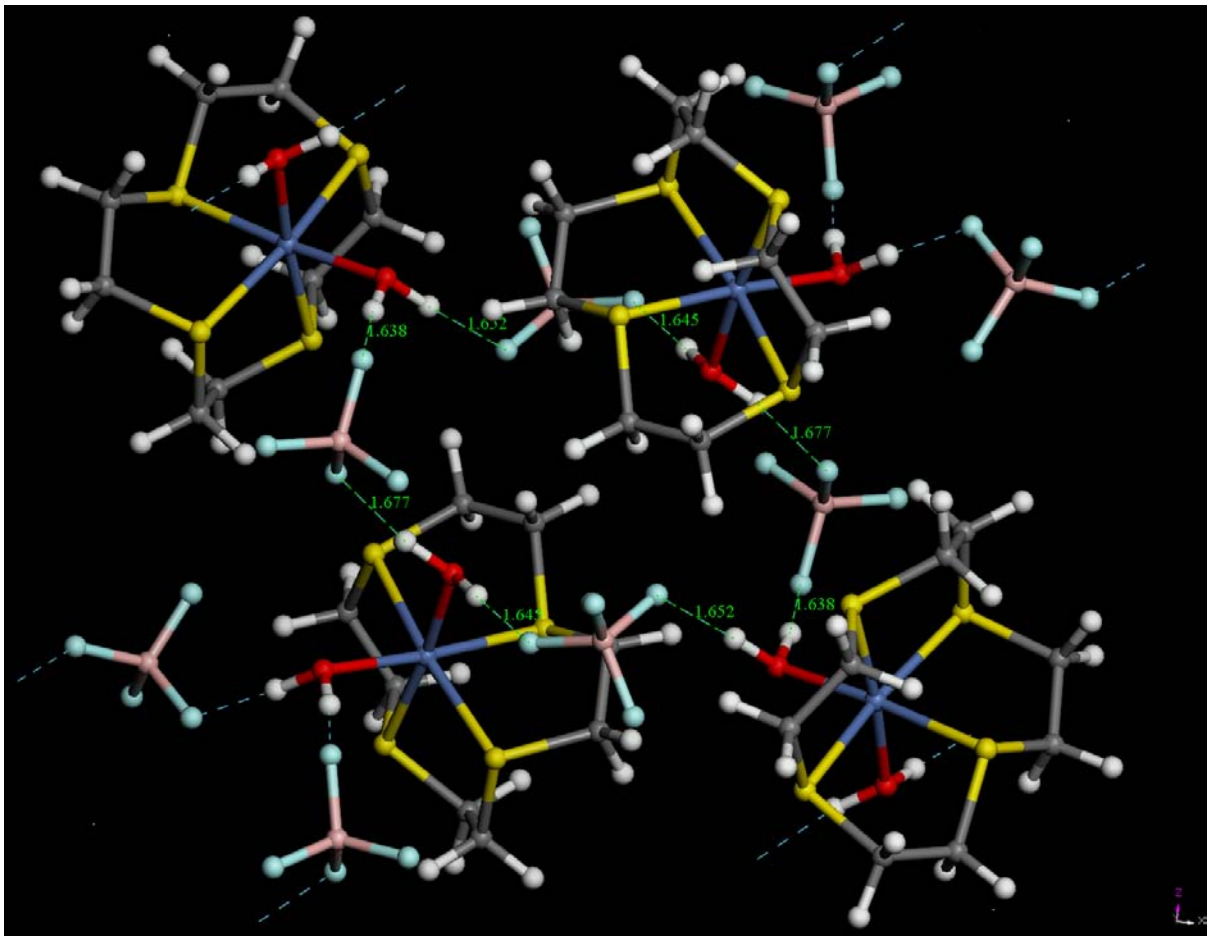

Figure S 13 The projection of the optimized crystal structure of 1·2H_2O on the crystallographic *ac* plane emphasizing the network of the hydrogen bonds in a ring; HF contacts are given in Å (green).

Following the optimizations, the single point energy calculations were performed at improved cutoff values up to 900 eV and denser k-point spacing of 0.15 $Å^{-1}$. The energies obtained were insensitive to k-point spacing but a marked energy decrease was observed for all species upon cutoff increase;

This journal is © The Royal Society of Chemistry 2012

the hydration energy was, however, fairly constant with respect to cutoff ranging from 1.489 eV to 1.495 eV (71.8–72.1 kJ/mol H_2O).

Table 1 Selected distances: Ni…B and O…F for **1** and **1**·$2H_2O$ from experiment used as initial structures and theory. There are two different BF_4 groups in both compounds hence two different sets of symmetry-related distances.

	Experiment			***Theory***		
	1	**1**·$2H_2O$		**1**	**1**·$2H_2O$	
	Ni…B (Å)	**Ni…B (Å)**	**O…F (Å)**	**Ni…B (Å)**	**Ni…B (Å)**	**O…F (Å)**
Symm related	3.823*	4.877	2.801	3.516*	4.828	2.631
	5.376	5.199	2.676	5.350	5.175	2.667
Symm related	4.792	4.786	2.781	4.920	4.788	2.646
	5.363	5.254	2.675	5.289	5.076	2.626

* note that the largest discrepancy between theory and experiment is for the secondary Ni…F contact; however, the calculations for **1** with enforced HS state of Ni(II) suggest that HS state and concomitant direct ligation of Ni(II) by BF_4^- anion, are not energetically favored.

This journal is © The Royal Society of Chemistry 2012

References

1 The proposed hydrogen bonding in **1**·2H_2O is strong and involves every hydrogen in water, which, we assert, would reduce the entropy of the water molecules in **1**·2H_2O to a negligible value relative to water vapor. Value taken from P.W. Atkins, *Physical Chemistry Sixth Edition*, OUP, Oxford, 1999, p. 926.

2 H. D. B. Jenkins, L. Glasser, *Inorg. Chem.* 2003, **42**, 8702.

3 K. Momma, F. Izumi, J. Appl. Crystallogr. 2008, **41**, 653.

4 C. F. Macrae, I. J. Bruno, J. A. Chisholm, P. R. Edgington, P. McCabe, E. Pidcock, L. Rodriguez-Monge, R. Taylor, J. van de Streek, P. A. Wood, *J. Appl. Cryst.* 2008, **41**, 466.

5 F. H. Allen, *Acta Cryst.* 2002, **B58**, 380.

6 Materials Studio ver. 5.0.0., Accelrys Software Inc., 2009.

7 M. J. Frisch, G. W. Trucks, H. B. Schlegel, G. E. Scuseria, M. A. Robb, J. R. Cheeseman, G. Scalmani, V. Barone, B. Mennucci, G. A. Petersson, H. Nakatsuji, M. Caricato, X. Li, H. P. Hratchian, A. F. Izmaylov, J. Bloino, G. Zheng, J. L. Sonnenberg, M. Hada, M. Ehara, K. Toyota, R. Fukuda, J. Hasegawa, M. Ishida, T. Nakajima, Y. Honda, O. Kitao, H. Nakai, T. Vreven, J. A. Montgomery, Jr., J. E. Peralta, F. Ogliaro, M. Bearpark, J. J. Heyd, E. Brothers, K. N. Kudin, V. N. Staroverov, T. Keith, R. Kobayashi, J. Normand, K. Raghavachari, A. Rendell, J. C. Burant, S. S. Iyengar, J. Tomasi, M. Cossi, N. Rega, J. M. Millam, M. Klene, J. E. Knox, J. B. Cross, V. Bakken, C. Adamo, J. Jaramillo, R. Gomperts, R. E. Stratmann, O. Yazyev, A. J. Austin, R. Cammi, C. Pomelli, J. W. Ochterski, R. L. Martin, K. Morokuma, V. G. Zakrzewski, G. A. Voth, P. Salvador, J. J. Dannenberg, S. Dapprich, A. D. Daniels, O. Farkas, J. B. Foresman, J. V. Ortiz, J. Cioslowski, D. J. Fox, Gaussian 09, Revision B.01, Gaussian, Inc., Wallingford CT, 2010.

8 G. Kresse, J. Furthmüller, Comput. Mater. Sci. 1996, **6**, 15; G. Kresse, J. Furthmüller, Phys. Rev. B 1996, **54**, 11169; G. Kresse, D. Joubert, Phys. Rev. B 1999, **59**, 1758.

9 P. E. Blöchl, Phys. Rev. B 1994, **50**, 17953.